

The turbulent cascade in five dimensions

José I. Cardesa^{1*}, Alberto Vela-Martín¹, Javier Jiménez¹

¹School of Aeronautics, Universidad Politécnica de Madrid, 28040 Madrid, Spain

*To whom correspondence should be addressed; E-mail: ji.cardesa@upm.es

To the naked eye, turbulent flows exhibit whirls of many different sizes. To each size, or scale, corresponds a fraction of the total energy resulting from a cascade in five dimensions: scale, time and three-dimensional space. Understanding this process is critical to strategies for modeling geophysical and industrial flows. By tracking the flow regions containing energy in different scales, we have detected the statistical predominance of a cross-scale link whereby fluid lumps of energy at scale Δ appear within lumps of scale 2Δ and die within those of scale $\Delta/2$. Our approach uncovers the energy cascade in a simple water-like fluid, offering insights for turbulence models while paving the way for similar analyses in conducting fluids, quantum fluids and plasmas.

Perhaps no other area of physics research has borne the influence of a rhyming verse more than turbulence, where Richardsons “*Big whirls have little whirls that feed on their velocity, and little whirls have lesser whirls and so on to viscosity*” (1) is embedded in the seminal theory of Kolmogorov, Onsager, von Weizsacker and Heisenberg (2, 3, 4, 5). The last three physicists transcribed the phenomenology in terms of wave numbers, which were to become the predominant tool in theoretical studies of the energy cascade (6, 7, 8, 9, 10). Consequently, scale and wavenumber became almost interchangeable concepts. A crucial point in the development of theories was the scale locality of the cascade, understood in terms of how close wavenumbers are when energy is exchanged between them (11). Since the advent of computer simulations, the locality of these wavenumber interactions has been controversial, with studies claiming evidence in favor of (12) or against (13) it. Rigorous explanations proposed for these discrepancies (14, 15) advocate for the classic scale-local view of the cascade. The debate, however, has turned predominantly around the equivalence between wavenumber and scale, ruling out any possibility of attributing the ongoing cascade to specific whirls visible where the flow actually evolves: the real space. Furthermore, computer simulations of industrial and atmospheric flows are carried out on numerical grids representing physical space and rely heavily on the modeling

of the interaction between the resolved (large) and subgrid (small) scales (16).

Studies of the interscale energy transfer based on real-space quantities share one of two limitations. They either focus on a subset of the source or sink terms responsible for the changes in energy at a point (17, 18), or they make no use of time thus precluding any dynamical information or knowledge of causality (19, 20, 21, 22, 23). Often both limitations are combined. A noteworthy exception found a delay in the peak of the correlation between energy at two different scales when following the larger-scale flow (24), suggesting that eddy structures transfer their energy to smaller scales. In the wake of that study, we aimed to follow individual eddy structures. This has become possible with modern data-storage facilities where flow simulations are preserved in a movie-like manner. Such data sets have enabled the verification of phenomenological descriptions that eventually feed into dynamical models.

We analyzed data from a direct numerical simulation of turbulence in a triply periodic cube, obtained by solving the Navier-Stokes equations for an incompressible fluid by means of a deterministically forced and statistically steady pseudo-spectral code (25). An important length scale in turbulent flows, η , is given by $\eta = \nu^{3/4}/\varepsilon^{1/4}$, where ν is the kinematic viscosity and ε is the mean rate of kinetic energy dissipation. This small-scale length is associated with the tiniest whirls of turbulence. Our $(2\pi)^3$ computational domain spanned $(1516\eta)^3$ in space and lasted 2090τ small-scale time units $\tau = \sqrt{\nu/\varepsilon}$. Expressed in terms of large-scale length and time units L_{int} and T_{int} (25), respectively, the simulation spanned $(5.3L_{int})^3$ and $66T_{int}$, with snapshots stored every 0.078τ . Although previous simulations surpassed our Reynolds number $L_{int}/\eta = 284$, our long yet temporally resolved dataset with a sizeable scale separation allowed us to statistically characterize a phenomenon by tracking many flow regions throughout their life.

The tracked flow regions that we now introduce in detail underpin our definition of whirls, or eddies. We isolated a range of scales by filtering the velocity fields with a spatial band-pass filter. Owing to the homogeneity of the flow, we used an isotropic filter to simplify the concept of scale to a single scalar Δ . We set the center of the filter band at the chosen scale Δ and used bands of constant width on a logarithmic scale (15). The upper and lower edges of the band resulted from subtracting two low-pass Gaussian filters (25). We focused on four scales from the geometric sequence $\Delta/\eta = (30, 60, 120, 240)$. This led to four time series of the dynamics of the flow, one for each scale. The object of our study was a scalar quantity, the kinetic energy, which evolved in time t , scale Δ , and three-dimensional space (x, y, z) . The kinetic energy at a scale is the sum of the squared filtered velocity components. The flow structures in Fig. 1 are geometrically connected regions of space where the energy is above a given threshold [Movie S1 (25)]. We chose the threshold systematically in the same way for all scales on the basis of the percolation properties of the energy at that scale (25, 26). We further time-tracked these flow objects using a technique developed for the tracking of coherent structures in turbulent channel

flows (27). Whereas generally an object was born small as the underlying energy exceeded the threshold and died small as its intensity decreased, an object often merged with or split from other objects during its life. We grouped objects related by a connection at some point in space-time within the same temporal graph (27). We called a graph emerging from this grouping an energy-eddy, or simply eddy, because it was educed according to the intense kinetic energy that it traced. We defined the scale of the eddy as the center Δ of the filter band that we used to compute it, the volume (V) as the sum of volumes of all objects of a graph existing at a given instant, and the lifetime (T_{life}) as the time elapsed between the birth and death of the first and last object within the graph, respectively.

The volume distributions collapsed onto a single curve over a fairly wide range (Fig. 2A) with scaling parameter Δ , after neglecting the tails. The lifetime distributions scaled with the local eddy turnover time $T_{eto} = \Delta^{2/3}\varepsilon^{-1/3}$ (Fig. 2B), found by assuming that for a range of scales where $L_{int} \gg \Delta \gg \eta$, the only relevant parameters are ε and Δ (2). The collapse of the probability density functions (Fig. 2B) supports that T_{eto} is indeed a scaling parameter over a range of lifetimes, excepting the short-lived small-scale eddies for which viscosity cannot be neglected. A log-normal distribution resulted from a nonlinear fit to all our data (Fig. 2B), where the mean and standard deviation were the fitting parameters minimizing the difference. The parameters were 0.8 and 1.3, respectively, so that the average eddy lifetime was of the order of T_{eto} . Overall, the picture that emerges lends support to the eddy definition based on the observed scaling properties of the eddy sizes and lifetimes.

Our four time sequences provide the space-time position of the eddies at four scales. By superposing contemporary fields from any two scales at a time, we linked those two scales by computing their intersection in space. We defined the intersection ratio for a single eddy of scale A intersecting N eddies of scale B at a given instant

$$R(A, B) \equiv \frac{\sum_i^N V_i(A \cap B)}{V(A)}, \quad (1)$$

where $V(A)$ is the volume of the eddy of scale A , and $V_i(A \cap B)$ is the intersection volume between the eddy of scale A and the i th intersected eddy of scale B (Fig. 3). This ratio is unity if the eddy of scale A is fully contained within one or more eddies of scale B , whereas it vanishes when $N = 0$ in the case of no intersections. We thus quantified how the field of scale- B eddies filled up individual eddies of scale A , which we followed.

We considered whether the intersections depended on the scale and on the stage in the life of the eddies. We split the lifetime of each scale- A eddy into equal fractions, or life stages. We then computed the mean intersection ratio $R_m(A, B)$ conditioned to a given life stage (25). We normalized the result by the corresponding null hypothesis (Fig. 4A), which showed intersection

levels higher than random for those scale combinations separated by a factor of 2 (orange and blue curves). The intersections between eddies of scales further apart did not show a trend that was distinctly different from the null hypothesis, indicating little or no spatial overlap. We then normalized the scale combinations separated by a factor of 2 with their corresponding maximum (Fig. 4B), which revealed that curves based on combinations where $A = 2B$ peaked towards the death of the scale- A eddies, whereas with $A = B/2$, the peak was closer to their birth. This statistical signature shows unequivocally how the eddies of a given scale originate from eddies of twice their scale, whereas they give rise to eddies half their scale before disappearing. This process replicated successively through four scales separated by a factor of 2, which suggests that a scale-local progression of the energy from the large to the small scales is, at the very least, a transited cascade path in homogeneous three-dimensional turbulence.

The results show that energy is transferred to the smaller scales overall. This average trend is often labelled as a forward, or direct, cascade. Some individual eddies, however, follow opposite paths. To illustrate this point, we used a crude definition of a forward cascade event as an individual eddy of scale A for which $R(A, B)$ averaged over the first half of T_{life} is larger than $R(A, B)$ averaged over the second half of T_{life} , taking $A = B/2$. This occurred twice as often as backscatter events, defined as eddies for which $R(A, B)$ was larger during the second half of T_{life} , where $A = B/2$. Even though this way of quantifying the predominance of forward cascade versus backscatter is somewhat simplistic, it is important to keep such event counts in mind because the trends that we observed (Fig. 4) should not obscure the underlying bidirectionality. Large-eddy simulations, which are extensively used in engineering and meteorological contexts, require particular attention to the direction of the energy flux between the resolved and subgrid scales (16).

Our analysis illustrated the locality of the energy exchanges and, more broadly, the phenomenology of the turbulent cascade. We looked for and verified this statistically in physical space with individual eddies of scales separated by factors of 2, 4, and 8. Future work could include studying the interaction between eddies separated by a factor of 3 or 1.5, together with a simulation at larger scale separations where the smallest scale is outside the viscous regime. Moreover, our approach has led to an observation and not to the identification of the physical process causing it. We can now, however, design a study targeting those regions in space-time where the energy cascade takes place to understand the causes. Lastly, our method was applied to a simple flow, but nothing prevents its use in more complicated cases with additional nonlinear terms. The presence of rotation, compressibility, conductivity, and quantum effects complicates the energy cascade considerably, leading to areas of turbulence research where Richardson’s verse is a more limited part of the story. Our approach could yield advances in those fields, particularly as the required data become available through numerical simulations (28, 29, 30).

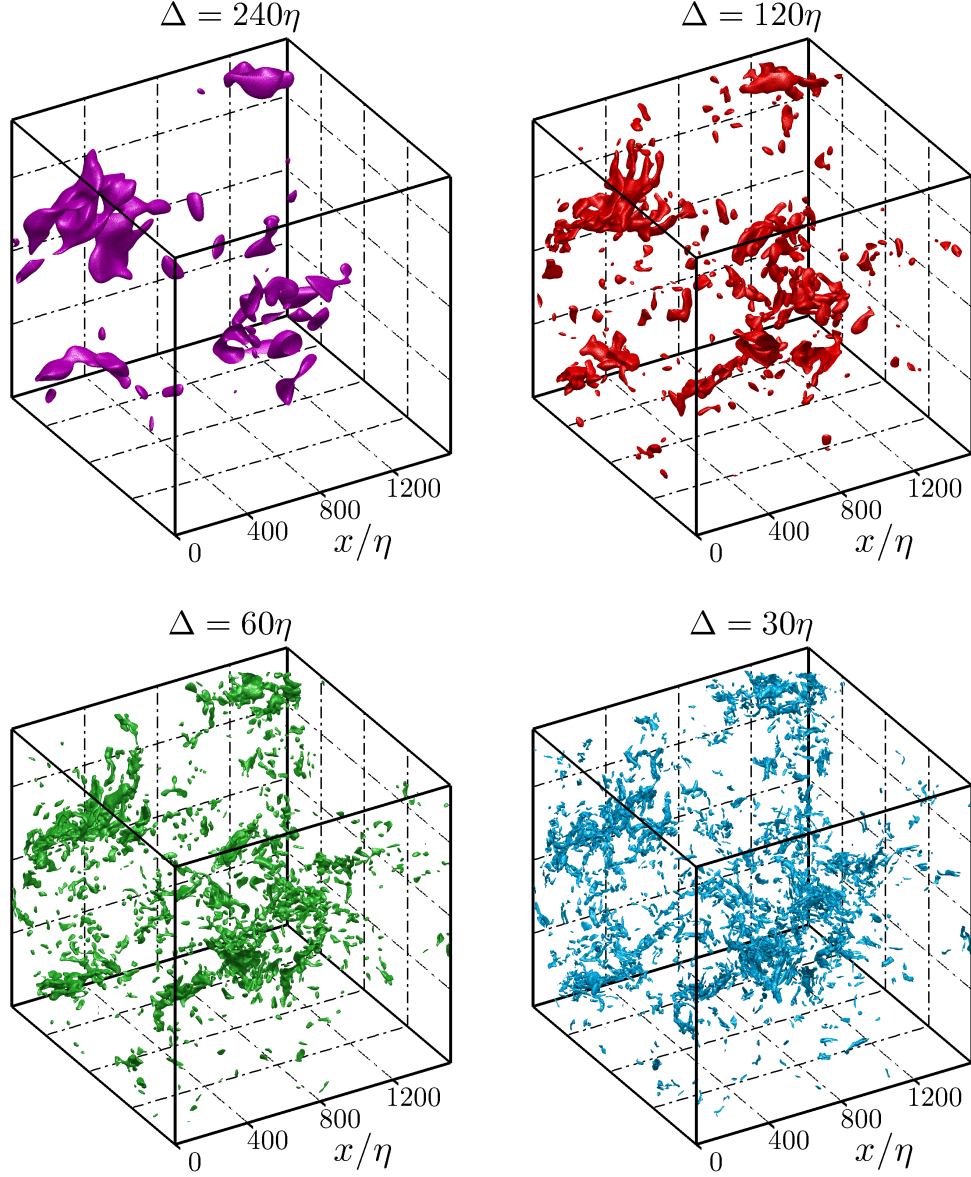


Figure 1: **Energy-eddies at four different scales Δ for the same instant in a numerical simulation of turbulence in a periodic cube.** A time sequence is shown in Movie S1 (25). The flow structures observed are the spatially connected regions of the flow where the energy at scale Δ is above a certain threshold (25).

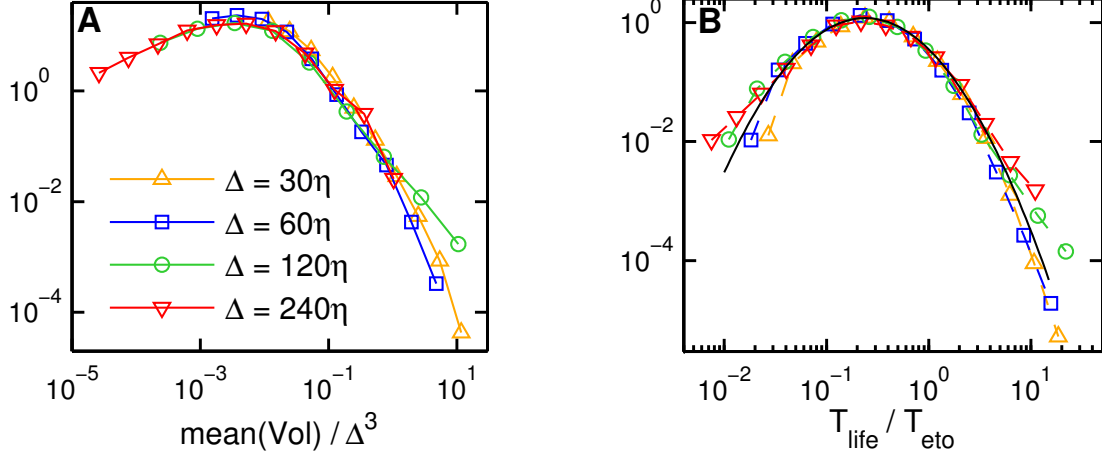


Figure 2: **Mean volumes and lifetimes of the eddies.** Probability density functions of (A) the mean volumes and (B) the lifetimes of the eddies. The solid black line in (B) follows a log-normal distribution with a mean of 0.8 and a standard deviation of 1.3. The volumes use for (A) are the average over each eddy's lifetime.

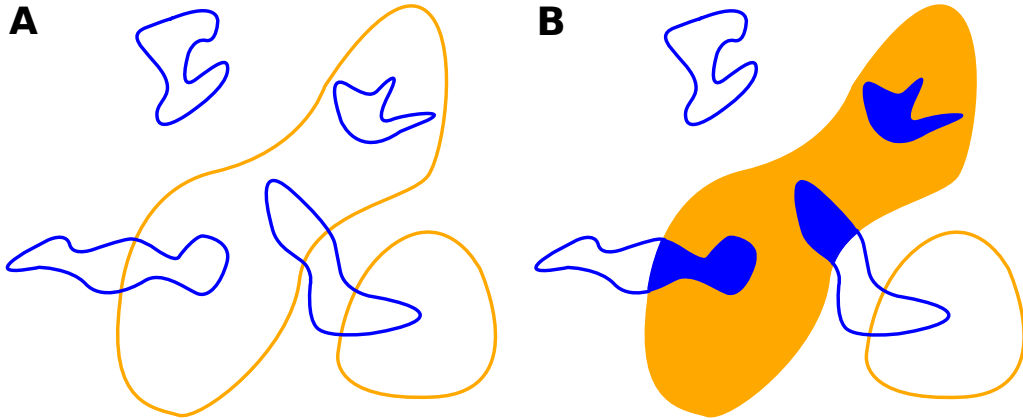


Figure 3: **Sketch illustrating the intersection ratio between eddies of scale A (orange) and B (blue).** $R(A, B)$ for the largest of the two eddies of scale A in (A) is given by the sum of the blue areas in (B), divided by the union of the blue and orange areas in (B).

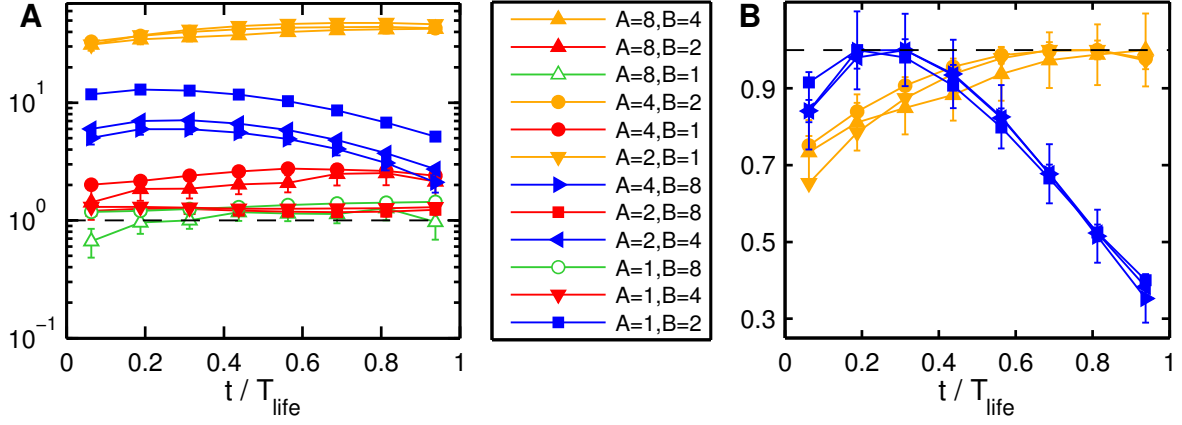


Figure 4: **Mean intersection ratio $R_m(A, B)$ between scales A and B at different stages of the lifetime of scale- A eddies.** Scales $\{1, 2, 4, 8\}$ in the legend correspond to $\Delta/\eta = \{30, 60, 120, 240\}$, respectively. **(A)** Normalized by the intersection level obtained by randomly locating fields B with respect to A (null hypothesis) (25). Unity implies a random intersection level. **(B)** Same as **(A)** but normalized by the maximum, keeping only A and B combinations separated by a factor of 2. Error bars in **(A)** and **(B)** represent 95% confidence intervals (31). The horizontal dashed line is located at unity.

References

1. L. F. Richardson, *Weather prediction by numerical process* (Cambridge University Press, 1922).
2. A. Kolmogorov, *Dokl. Akad. Nauk SSSR* **30**, 299 (1941).
3. L. Onsager, *Il Nuovo Cimento (1943-1954)* **6**, 279 (1949).
4. C. F. Weizsäcker, *Zeitschrift für Physik* **124**, 614 (1948).
5. W. Heisenberg, *Zeitschrift für Physik* **124**, 628 (1948).
6. A. M. Obukhoff, *Dokl. Akad. Nauk SSSR* **32**, 22 (1941).
7. R. H. Kraichnan, *Journal of Fluid Mechanics* **5**, 497 (1959).
8. C. Leith, *Physics of Fluids* **10**, 1409 (1967).
9. I. Proudman, W. H. Reid, *Philosophical Transactions of the Royal Society of London A* **247**, 163 (1954).
10. T. Tatsumi, *Proceedings of the Royal Society of London A* (1957), vol. 239, pp. 16–45.
11. R. H. Kraichnan, *Journal of Fluid Mechanics* **47**, 525 (1971).
12. J. A. Domaradzki, W. Liu, M. E. Brachet, *Physics of Fluids* **5**, 1747 (1993).
13. P. K. Yeung, J. G. Brasseur, *Physics of Fluids* **3**, 884 (1991).
14. G. L. Eyink, H. Aluie, *Physics of Fluids* **21**, 115107 (2009).
15. H. Aluie, G. L. Eyink, *Physics of Fluids* **21**, 115108 (2009).
16. P. Sagaut, *Large eddy simulation for incompressible flows: an introduction* (Springer Science & Business Media, 2006).
17. M. Wan, Z. Xiao, C. Meneveau, G. L. Eyink, S. Chen, *Physics of Fluids* **22** (2010).
18. J. I. Cardesa, A. Vela-Martín, S. Dong, J. Jiménez, *Physics of Fluids* **27**, 111702 (2015).
19. T. Aoyama, *et al.*, *Journal of the Physical Society of Japan* **74**, 3202 (2005).
20. U. Piomelli, W. Cabot, P. Moin, S. Lee, *Physics of Fluids* **3**, 1766 (1991).
21. S. Cerutti, C. Meneveau, *Physics of Fluids* **10**, 928 (1998).
22. P. A. Davidson, B. R. Pearson, *Physical Review Letters* **95**, 214501 (2005).

23. R. J. Hill, *Journal of Fluid Mechanics* **468**, 317 (2002).
24. C. Meneveau, T. S. Lund, *Physics of Fluids* **6**, 2820 (1994).
25. Materials and methods, along with a movie, are available as supplementary materials.
26. F. Moisy, J. Jiménez, *Journal of Fluid Mechanics* **513**, 111 (2004).
27. A. Lozano-Durán, J. Jiménez, *Journal of Fluid Mechanics* **759**, 432 (2014).
28. J. C. Perez, J. Mason, S. Boldyrev, F. Cattaneo, *Physical Review X* **2**, 041005 (2012).
29. N. Navon, A. L. Gaunt, R. P. Smith, Z. Hadzibabic, *Nature* **539**, 72 (2016).
30. M. Wan, *et al.*, *Physics of Plasmas* **23**, 042307 (2016).
31. L. H. Benedict, R. D. Gould, *Experiments in fluids* **22**, 129 (1996).
32. S. A. Orszag, G. S. Patterson, *Physical Review Letters* **28**, 76 (1972).
33. S. Pope, *Turbulent Flows* (Cambridge University Press, 2000).

Acknowledgments

We thank A. Lozano-Durán for providing the code for the tracking of flow structures. All authors acknowledge funding from project COTURB (Coherent Structures in Wall-bounded Turbulence) of the European Research Council. The data for this study were obtained using the DECI-PRACE (Distributed European Computing Initiative-Partnership for Advanced Computing in Europe) resource Minotauro based in Spain at the Barcelona Supercomputing Centre. M.P. Encinar helped making the data public. The flow fields are freely available from our online database at <https://torroja.dmt.upm.es/turbdata/Isotropic>.

List of supplementary materials

Materials and Methods

Figs. 5 to 10

Table 1

References (32, 33)

Movie 1

Supplementary materials

Materials and Methods

Numerical simulation The Navier-Stokes equations for an incompressible Newtonian fluid are given by

$$\left(\frac{\partial}{\partial t} + u_j \frac{\partial}{\partial x_j} \right) u_i = - \frac{\partial}{\partial x_i} (p/\rho) + \nu \frac{\partial^2 u_i}{\partial x_j \partial x_j} + f_i$$

$$\frac{\partial u_i}{\partial x_i} = 0,$$

where u_i and f_i are the i -th components of the velocity and forcing, respectively, p is the pressure, ρ is the density, ν is the kinematic viscosity, t is time, x_i spans the three spatial directions and summation over repeated indices is implied. Our solver integrated a Fourier-transformed version of these equations using a third-order Runge-Kutta scheme in time and a pseudo-spectral treatment of the triply periodic domain (32). Each side span $L_d = 2\pi$ and was discretized with $N = 1024$ collocation points. The forcing vector \widehat{f}_i , where the hat denotes Fourier transform, followed

$$\widehat{f}_i(\mathbf{k}, t) = \begin{cases} \varepsilon \widehat{u}_i(\mathbf{k}, t) / [2E_f(t)], & \text{if } 0 < k < k_f, \\ 0, & \text{otherwise,} \end{cases}$$

where $\varepsilon \equiv 1$ is the intended space-time mean dissipation $\frac{\nu}{2} \left\langle \left(\frac{\partial u_i}{\partial x_j} + \frac{\partial u_j}{\partial x_i} \right)^2 \right\rangle$, \mathbf{k} is the wave vector, $k = |\mathbf{k}|$, $E_f(t) = \int_0^{k_f} E(k, t) dk$ and $k_f = 4\pi/L_d$. The spatial resolution was set to $k_{max}\eta = 2$ where $k_{max} \equiv \sqrt{2}N/3$, leading to $Re_\lambda = 315$, $L_{int} = 1.18$. Quantities $E(k, t)$, L_{int} , and Re_λ are defined as in equations (6.188), (6.225) and (6.63) of Pope (33). Quantity T_{int} used in the manuscript is defined as $T_{int} \equiv L_{int}/\sqrt{2K/3}$, where $K \equiv \langle u_i u_i \rangle / 2$ is the space-time mean kinetic energy. Phase-shifts were used for the dealiasing. The numerical code was parallelized using a hybrid CUDA-MPI implementation and ran on 64 NVIDIA GPUs in the Barcelona Supercomputing Centre (Spain).

Band-pass filtering To isolate a range of scales in the vicinity of Δ , we combined two Gaussian low-pass filters with filter widths Δ_1 and Δ_2 as follows:

$$G_\Delta(r) = \left(\frac{10}{\pi} \right)^{3/2} \left[\frac{1}{\Delta_1^3} \exp\left(-\frac{10r^2}{\Delta_1^2} \right) - \frac{1}{\Delta_2^3} \exp\left(-\frac{10r^2}{\Delta_2^2} \right) \right],$$

where

$$\Delta_1 < \Delta < \Delta_2 ; \quad \Delta_2 = 2\Delta_1 ; \quad \Delta = \sqrt{2}\Delta_1 ; \quad r^2 = r_i r_i.$$

The filtered velocity components $\bar{u}_i(\mathbf{x}) = \int G_\Delta(r) u_i(\mathbf{x} - \mathbf{r}) d\mathbf{r}$ were computed in Fourier space as $\widehat{\bar{u}}_i(\mathbf{k}) = \widehat{G}_\Delta(k) \widehat{u}_i(\mathbf{k})$, where $\widehat{G}_\Delta(k) = \exp(-(k\Delta_1)^2/40) - \exp(-(k\Delta_2)^2/40)$. The spectra of the energy at each of the four chosen Δ are shown on Fig. 5.

Thresholding We studied the flow regions with energy above the threshold $\theta_\Delta = \mu_\Delta + H_\Delta \sigma_\Delta$, where μ_Δ and σ_Δ are the mean and standard deviation, respectively, of the energy at scale Δ . For a range of H_Δ , we gathered two quantities: the ratio of the largest eddy divided by the sum of all eddies, which we call ϕ , and the number of eddies ψ . The percolation properties of the energy can be characterized (26) by $\phi(H_\Delta)$ and $\psi(H_\Delta)$, which we show on Fig. 6 for $\Delta/\eta = 60$ - we found similar curves at the other Δ/η . We define the critical H_Δ^* as the point where the rate of decrease in $\phi(H_\Delta)$ is greatest, shown as a dashed vertical line on Fig. 6. The corresponding thresholds θ_Δ^* were set as reference, and we carried out the analysis reported in this manuscript at 3 thresholds for each scale: $\theta_\Delta = \{\theta_\Delta^*, \sqrt{2}\theta_\Delta^*, 2\theta_\Delta^*\}$. The eddy structures contain a fraction of the flow's volume and energy which are given in Table 1 for each θ_Δ used, along with the corresponding number of graphs. The results presented in the manuscript are all based on the highest threshold $2\theta_\Delta^*$. Figure 2A is reproduced at the two lower thresholds in Fig. 7, while Fig. 2B is reproduced in Fig. 8 at the two lower thresholds. The conclusions drawn from these two figures remain qualitatively unaltered by the threshold. Figure 4A was found to depend on the threshold as shown on Fig. 9. We found the reason for this dependency to be the creation, at the two lower thresholds, of a single graph percolating the entire time series, with more than 90% of the volume in the flow structures belonging to the largest graph - see Fig. 10. This influenced significantly the intersection ratio computations due to most structures being part of the same (largest) graph.

Mean intersection $R_m(A, B)$ We split T_{life} for each scale- A eddy into 8 equal fractions, or life stages, which are the same regardless of T_{life} . We then compute for each scale- A eddy the mean of $R(A, B)$ over each of its life stages, obtaining a single 8-point series $\langle R(A, B) \rangle$ for each eddy which corresponds to a set of life stages that is common across all scale- A eddies. In the next step, we compute the mean of $\langle R(A, B) \rangle$ averaged over all scale- A eddies for a given life stage. In this way we obtain the mean intersection ratio $R_m(A, B)$ as a function of where scale- A eddies are with respect to their life. We focus on those scale- A eddies with lifetimes in the range $1/4 < T_{life}/T_{eto} < 2.5$, which contains the PDFs on Fig. 2B from their mode to ten times the mode. This range keeps approximately 50% of the graphs and the best collapsed portion of the PDFs. We apply the lifetime restriction only to field A , while we keep all eddies from field B when computing the intersections. The trend in Fig. 4B persisted as we narrowed the range of admitted lifetimes for scale- A eddies, so that comparing eddies of scale A with lifetimes spread over a factor of up to 10 did not alter our main conclusion.

Null hypothesis of $R_m(A, B)$ The intersection ratio $R(A, B)$ between a scale- A eddy and a field of randomly located scale- B eddies occupying $\sum V_B$ is taken as the volume fraction given by $(\sum V_B)/(8\pi^3)$, where $8\pi^3$ is the volume of the computational domain.

Temporal resolution The temporal resolution between the conserved velocity fields of the simulation was 0.078τ . We found, however, that one in every three fields could be used for the

tracking. With this coarser temporal resolution of 0.235τ , less than 0.5% of the total volume of the tracked structures with the finest Δ was lost, while the processing cost was significantly reduced.

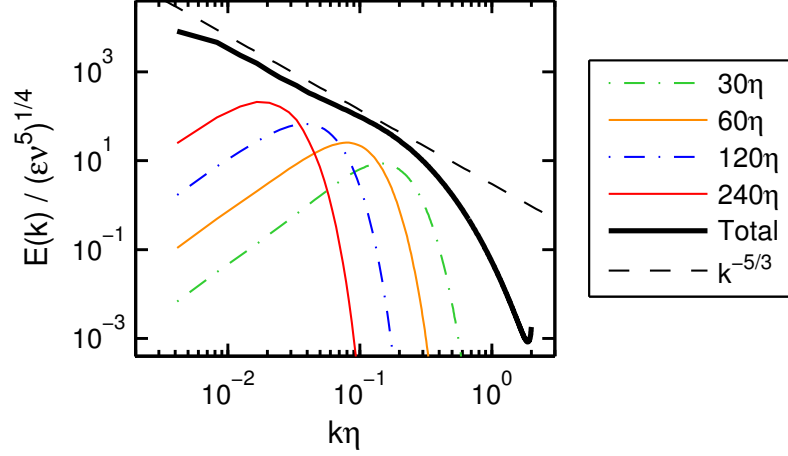


Figure 5: Energy spectra of the band-pass filtered velocities at different scales. Black thick solid line shows the energy spectrum of the unfiltered velocity.

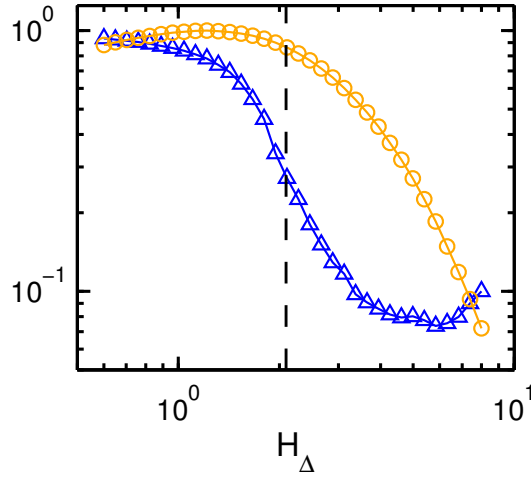


Figure 6: Percolation properties of the energy field at $\Delta = 60\eta$. Blue triangles show $\phi(H_\Delta)$ and orange circles show $\psi(H_\Delta) / \max(\psi)$. The vertical dashed line shows θ_Δ^* for this Δ .

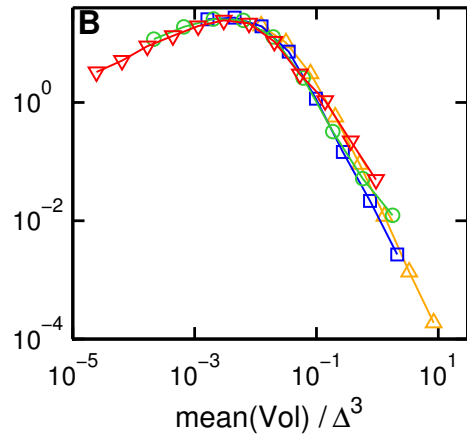
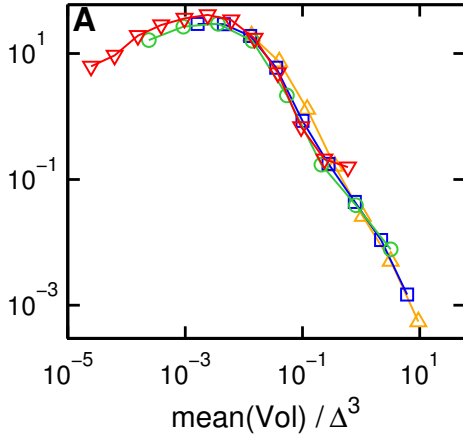


Figure 7: Identical to Fig. 2A for thresholds (A) θ_{Δ}^* (B) $2^{1/2}\theta_{\Delta}^*$.

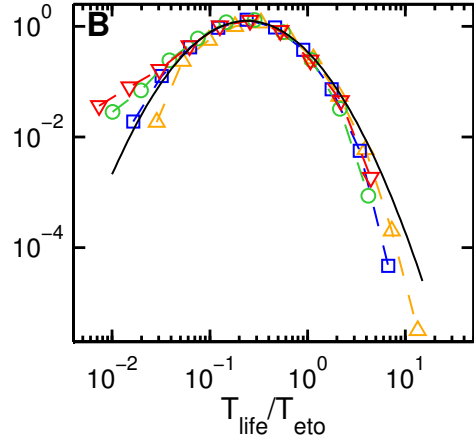
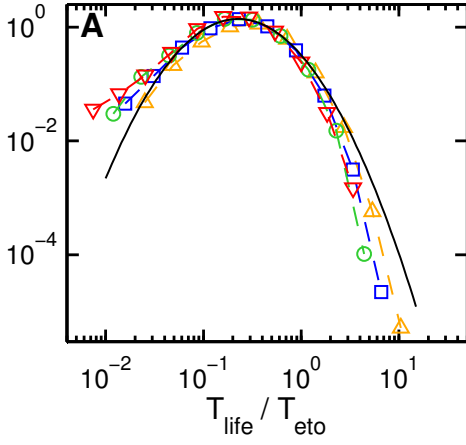


Figure 8: Identical to Fig. 2B for thresholds (A) θ_{Δ}^* (B) $2^{1/2}\theta_{\Delta}^*$.

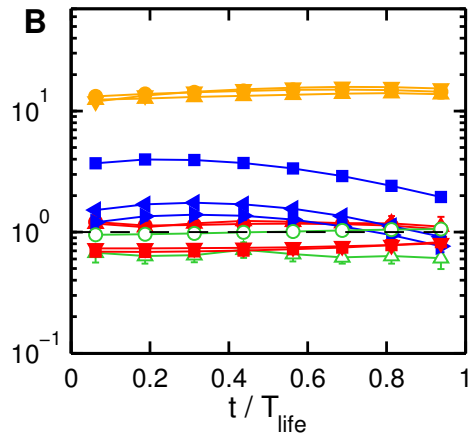
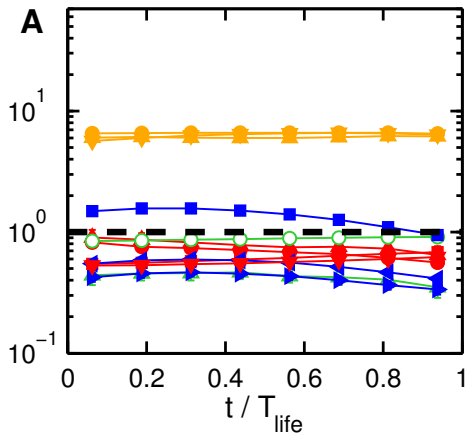


Figure 9: Identical to Fig. 4A, with same color legend and for thresholds (A) θ_{Δ}^* (B) $2^{1/2}\theta_{\Delta}^*$.

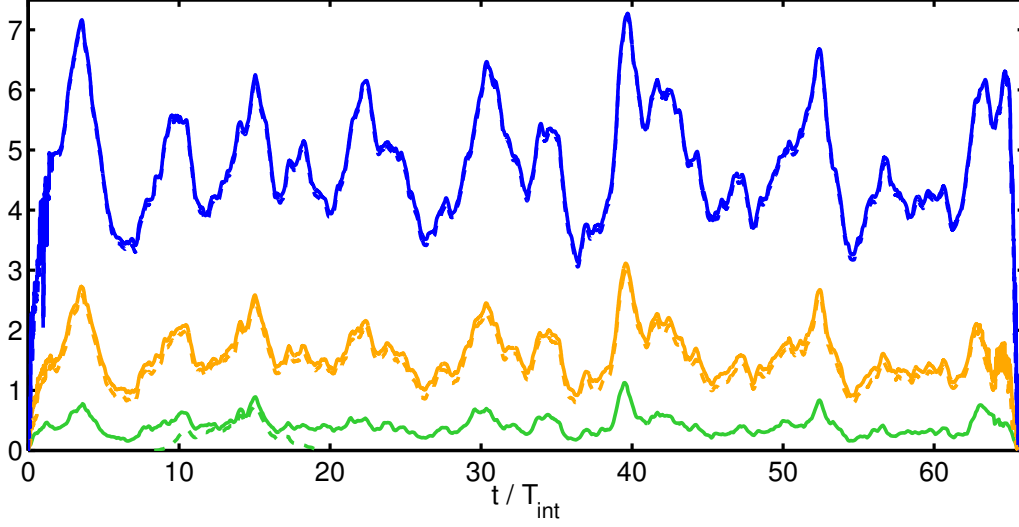


Figure 10: Time-dependence of the volume of the largest graph (dotted lines) and of the sum of all graphs (solid lines) during the simulation, normalized by the domain volume [%]. Different colors correspond to different thresholds: blue θ_{Δ}^* , orange $(2^{1/2}\theta_{\Delta}^*)$, green $(2\theta_{\Delta}^*)$. Results shown for scale $\Delta = 120\eta$, we found similar curves at the other Δ .

Δ/η	% energy			% volume			number of graphs		
	θ_{Δ}^*	$\sqrt{2}\theta_{\Delta}^*$	$2\theta_{\Delta}^*$	θ_{Δ}^*	$\sqrt{2}\theta_{\Delta}^*$	$2\theta_{\Delta}^*$	θ_{Δ}^*	$\sqrt{2}\theta_{\Delta}^*$	$2\theta_{\Delta}^*$
240	21.8	9.2	2.6	6.1	2	0.4	3.8×10^3	4.5×10^3	2.9×10^3
120	21.1	9.9	3.5	5	1.8	0.5	4.7×10^4	4.7×10^4	3.1×10^4
60	19.6	9.5	3.7	4.1	1.5	0.4	4.0×10^5	3.6×10^5	2.4×10^5
30	18.5	9.6	4.2	3.2	1.2	0.4	1.4×10^6	1.3×10^6	8.8×10^5

Table 1: Fraction of energy and volume contained in the educed objects and number of educed graphs for the filter scales and thresholds used in our study.